Effect of the 2018 Martian global dust storm on the CO2 density in the lower nightside thermosphere observed from MAVEN/IUVS Lyman-alpha absorption

Jean-Yves Chaufray, M. Chaffin, Justin Deighan, S. Jain, N. Schneider, M. Mayyasi, B. Jakosky

Effect of the 2018 Martian global dust storm on the CO_2 density in the lower nightside thermosphere observed from MAVEN/IUVS Lyman-alpha absorption

J-Y. Chaufray[1], M. Chaffin[2], J. Deighan[2], S. Jain[2], N. Schneider[2], M. Mayyasi[3], and B. Jakosky[2]

[1] LATMOS/IPSL, CNRS, UVSQ Université Paris-Saclay, Sorbonne Université, Guyancourt, France

[2]LASP, University of Colorado Boulder, Boulder, Colorado, USA

[3]Center for Space Physics, Boston University, Boston, Massachusetts, USA

Abstract

The MAVEN/IUVS instrument measures Lyman-α emissions from interplanetary and martian hydrogen at the limb and through the extended corona of Mars. In June 2018, a Global Dust Storm (GDS) surrounded Mars for a few months, heating the lower atmosphere and leading to an expansion of the Martian atmosphere. Nightside IUVS observations before and throughout this GDS showed the altitude of CO_2 absorption of Lyman-α photons in the thermosphere to increase by 4.5±1.0 km on 8 June 2018. This shift is attributed to an increase of the CO_2 density by a factor 1.9±0.2 at 110 km due to the heating of the lower atmosphere. These nightside observations, not previously used to study dust storms, in an altitude range not sampled by other instruments, are consistent with dayside MAVEN observations and allow for more comprehensive determination of the global changes produced by the GDS on the Martian thermosphere.

1) Introduction

Absorption of UV photons in the Martian upper atmosphere is the main source of thermospheric heating as well as of ionization, dissociation and excitation of CO_2 molecules (e.g. Fox et al. 2008). The partial absorption of the UV solar or stellar photons can also be used by remote sensing instrument to derive the density, temperature or composition of the Martian thermosphere as done by Mars Express/SPICAM (e.g. Forget et al. 2009) and more recently by MAVEN/IUVS (Gröller et al. 2015, 2018). Another method used to derive the CO_2 density in the Martian nightside thermosphere near 110 km utilizes the absorption by CO_2 of Lyman-α photons emitted in the interplanetary medium and Martian exosphere (Bertaux et al. 2005, Chaufray et al. 2011). Chaufray et al. (2011) used this method to derive seasonal variations of lower thermospheric nightside CO_2 density that were in good agreement with variations deduced from stellar occultations. This method was shown to be less accurate than the stellar/solar occultation method because it is based on only one wavelength instead of the full UV spectral range for occultations, yet it has the advantage of simplicity due to requiring fewer constraints on pointing, and portability to any latitudes, longitudes, and local time at nightside compared with terminator-limited solar occultations. In June 2018, an intense Global Dust Storm (GDS) surrounded Mars lasting a few months, heating the lower atmosphere (Kass et al. 2018) and led to an expansion of the Martian atmosphere by few kilometers at thermospheric altitudes (Bougher et al., 2019, see also Jain et al. this issue, and Elrod et al this issue). Since Lyman-α absorption occurs in the lower thermosphere, an increase of CO_2 density at a given altitude during the GDS would be expected to increase the altitude of Lyman-α absorption by CO_2. In this paper, MAVEN/IUVS nightside "limb scans" are used to estimate the increase of the CO_2 density at 110 km produced by this GDS. Section 2 describes the dataset and assumptions used to derive the CO_2 density. In section 3 the variations of CO_2 density at 110 km during the dust storm are shown. The results are compared to dayside variations observed by other instruments in section 4.

2) Data analysis

At the beginning of the global dust storm, the MAVEN spacecraft periapsis was on the dayside, and its apoapsis on the nightside. The IUVS “coronal scans” occur on the inbound and outbound segments of the orbit from periapsis (McClintock et al. 2015). During these parts of MAVEN’s orbit, the Lyman-α emission of atomic hydrogen is observed scanning the limb with tangent altitudes ranging from below the planet’s surface up to the exosphere ~ 3400 km. During the outbound leg, the spacecraft was partly in the dayside on 8 June 2018 and in the nightside during the inbound leg. In this paper, the nightside inbound observations from MAVEN/IUVS where the solar zenith angle of the tangent point is larger than ~90° and the solar zenith angle of the spacecraft is larger than 90° are used. The geometry of one observation is displayed on Fig. 1

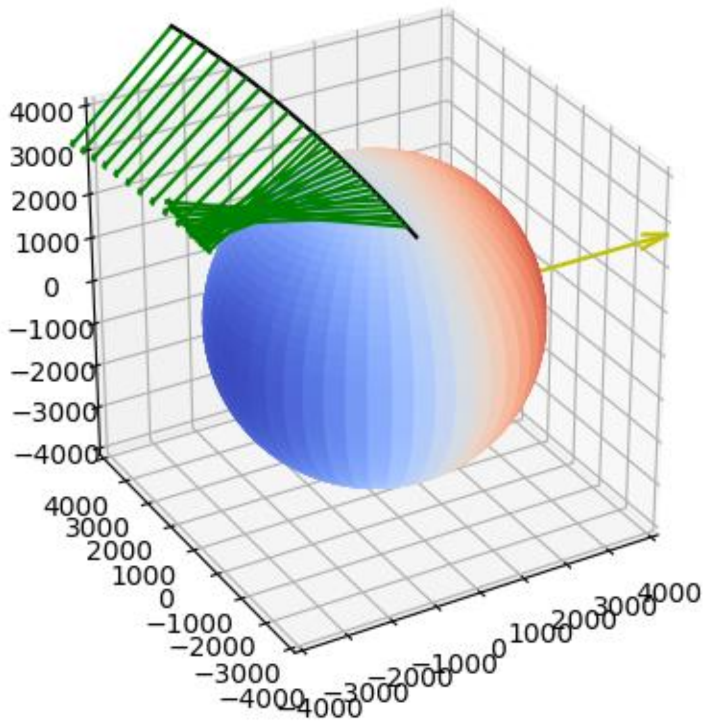

Figure.1 Geometry of the observation during orbit 7178 in the Mars Sun Orbit (MSO) frame.All axis are in km. The Martian surface is red at the dayside and blue at the nightside. MAVEN is moving toward is pericenter and its position during the observation is represented by the black solid line. The lines of sight of IUVS during the different inlimb scans are represented in green. The sun direction is shown by the yellow arrow (X axis).

Atmospheric hydrogen is not directly illuminated by the Sun in the shadow, and the brightness dispersion at a given tangent altitudes is smaller on the nightside than on the dayside, making the CO_2 density retrieval easier. In this study, we only use observations with a tangent altitude spanning the surface to 250 km (files tagged “inlimb” in the Planetary Data System archives). The resulting observations include 33 non-consecutive orbits spanning orbit # 7106 (25 May

2018) to orbit # 7256 (22 June 2018). Six inbound limb scans are done in each orbit with a sampling of approximatively 10 km. 7 spatial bins are transmitted per limb scan, leading to 42 individual limb profiles per orbit. The latitude, longitude, SZA and local time ranges at the tangent point covered for each orbit are given in Table 1

# Orbit	Day	Ls	SZA	Latitude	E Longitude	Local Time
7106	25 May	181.5	117-138	27-55	49-74	20.8-22.7
7112	26 May	182.2	117-138	29-55	17-42	20.8-22.6
7116	27 May	182.6	117-137	30-54	115-140	20.6-22.5
7120	27 May	183.0	118-137	26-54	215-239	20.5-22.4
7124	28 May	183.5	118-137	26-53	313-338	20.4-22.3
7128	29 May	183.9	118-136	25-53	52-76	20.4-22.2
7132	30 May	184.3	118-136	24-52	151-174	20.3-22.1
7136	30 May	184.7	118-135	23-52	250-273	20.2-22.1
7140	31 May	185.1	118-135	22-51	349-12	20.2-22.0
7144	01 Jun	185.6	117-134	22-51	88-111	20.1-21.9
7150	02 Jun	186.2	117-133	22-50	56-79	20.0-21.8
7154	03 Jun	186.6	117-132	21-49	155-177	20.0-21.7
7158	04 Jun	187.1	117-131	21-49	254-276	19.9-21.6
7162	04 Jun	187.5	116-131	20-48	353-15	19.8-21.5
7166	05 Jun	188.0	115-130	19-48	91-113	19.7-21.4
7170	06 Jun	188.3	115-129	19-47	190-211	19.7-21.3
7174	06 Jun	188.8	113-128	18-46	290-310	19.6-21.2
7178	07 Jun	189.2	112-127	18-45	28-49	19.5-21.2
7182	08 Jun	189.6	112-127	17-45	126-148	19.5-21.2
7198	11 Jun	191.4	108-124	15-43	162-182	19.2-20.7
7202	12 Jun	191.8	107-124	15-43	261-281	19.1-20.7
7208	13 Jun	192.4	106-123	14-42	230-250	19.0-20.6
7212	14 Jun	192.9	105-123	13-41	329-348	19.0-20.5
7216	14 Jun	193.3	104-122	13-41	67-87	18.9-20.4
7222	15 Jun	194.0	103-121	12-40	36-55	18.8-20.3
7226	16 Jun	194.4	102-120	11-39	135-154	18.7-20.2
7230	17 Jun	194.8	101-120	11-39	235-253	18.6-20.1
7234	18 Jun	195.3	99-119	10-38	333-352	18.6-20.1
7238	18 Jun	195.7	98-118	10-37	72-91	18.5-20.0
7244	19 Jun	196.4	97-117	10-37	41-59	18.4-19.9
7248	20 Jun	196.8	96-116	8-36	139-158	18.3-19.8
7252	21 Jun	197.2	95-115	8-36	239-257	18.2-19.7
7256	22 Jun	197.7	93-115	7-35	338-357	18.2-19.6

Table 1 : MAVEN orbits used for this study (column 1). The spatial/temporal information for each orbits are also given. Solar Zenith Angla (SZA), latitude, East longitude and local time

range refers to the tangent point of the different lines of sight. The MAVEN orbits drift in longitude by ~ 115°/orbit due to the Martian rotation.

The spacecraft altitude varies between 2100 to 3400 km during these 6 inbound limb observations. During these observations, the approximate distance between the spacecraft and the tangent point is ~ 5000 km. The IUVS slit projection is normal to the orbit of MAVEN (perpendicular to the vertical direction). The IUVS spatial bins (corresponding to a binning of 115 physical pixels along the slit) projection at the tangent point is ~ 20 km.

The 42 individual limb profiles for orbit #7178 are displayed in Figure 2. For all the orbits, the variations of the brightness between the different limb scans (~ 0.14kR) is close to the error bar of the individual measurement (~0.13 kR). There are small variations of sensitivity between the different spatial bins along the slit, but we do not apply any flatfield corrections in this study, because our results are not sensitive to the absolute sensitivity of the spatial bins. We average the profiles to increase the signal to noise. Profiles are averaged every 8 km. The average profile is shown in Figure. 2.

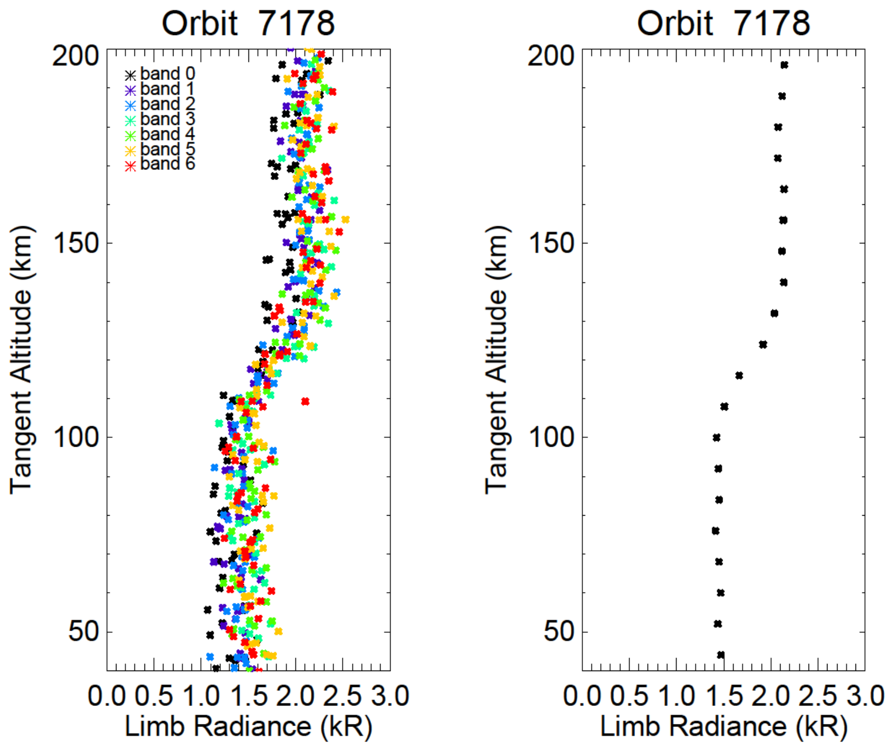

Figure. 2 : Left : Vertical profiles of the H Lyman-α brightness measured at limb between 40 and 200 km for each of 7spatial bins (labeled as "bands" and shown with different colors) during orbit 7178 for all six inbound limb scans, observed on 7 June 2018. The error bar for each individual value is ~ 0.13 kR. Right : Average profile derived with a vertical resolution of 8 km. The uncertainty on the mean is ~ 0.03 kR, lower than the thickness of the points.

The brightness between 160 and 200 km is approximately constant in the profiles shown in Figure 2. The brightness between 40 and 80 km is also constant. The vertical variation of the brightness is well described by the formulation in Equation 1 (see Chaufray et al., 2011):

$$I(z) = I_0 + (I_1 - I_0)\exp(-\tau_{CO2}(z)) \qquad (1)$$

where $\tau_{CO2}(z)$ is the slant path integrated atmospheric transmittance by CO_2 at tangent altitude z, I_0 is the average brightness between 40 and 80 km, I_1 is the average brightness between 160 and 200 km. I_0 corresponds to Lyman-α photons emitted between the spacecraft and the absorption layer, i.e. the region below 100 km, $I_1 - I_0$ corresponds to the contribution of photons mostly emitted above the absorption layer, in the solar illuminated side of the line of sight . These photons are absorbed or "occulted" by the atmospheric CO_2 for z lower than 100 km (where $\tau_{CO2} >> 1$), not absorbed for z > 160 km (where $\tau_{CO2} << 1$), and partly absorbed in between.

For each observation, a normalized brightness or transmission function (Equation 2) can be deduced. As the transmission function computed from stellar occultation (e.g. Quémerais et al. 2006), this function is independent of the absolute calibration of the instrument as long as the sensitivity doesn't drift over time of the observation.

$$T(z) = \frac{I(z) - I_0}{I_1 - I_0} = e^{-\tau_{CO2}} \qquad (2)$$

An example of transmission function is displayed in Figure 3 for orbit #7178

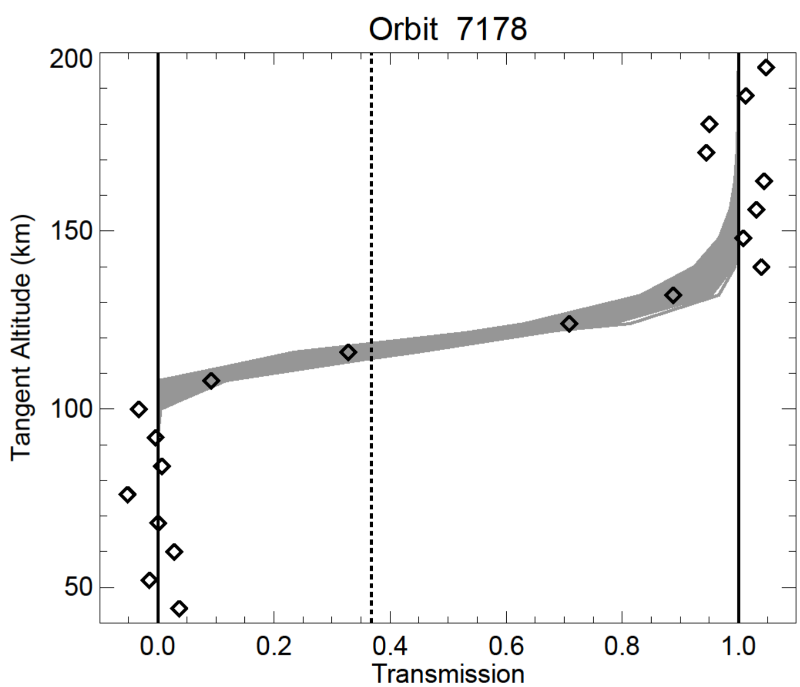

Fig. 3 Transmission function for orbit 7178 (diamonds) and the best fit derived using a function given by Eq. 3 (solid line). The two vertical solid lines indicate Transmission= 0 and Transmission =1. The vertical dotted line indicate Transmission = e^{-1}. Because I_0 and I_1 are average values between 40-80 km and 160-200 km respectively, the computed individual transmission values can be < 0 (when $I(z) < I_0$) near 100 km and > 1 (when $I(z) > I_1$) near 160 km respectively.The best fits obtained from a Monte Carlo error analysis are also displayed by the grey area.

A theoretical expression of the CO_2 absorption optical thickness can be derived assuming an isothermal absorption layer between 100 and 160 km (Equation 3).

$$\tau_{CO2}(z) = n(z)H\sqrt{\frac{2\pi R}{H}}\sigma = n(z_0)H\sqrt{\frac{2\pi R}{H}}\sigma \exp\left[-\frac{(z-z_0)}{H}\right] \qquad (3)$$

The isothermal assumption is justified at the nightside, given the limited accuracy of the method. In Equation 3, $n(z)$ is the CO_2 density at the tangent point altitude z, H the scale height of the CO_2 density, σ is the CO_2 absorption cross section at 121.6 nm (equal to $6.2\text{x}10^{-20}$ cm^2), the product $n(z)H$ is the column density above z and the factor $(2\pi R/H)^{1/2}$ is the approximate ratio of the limb length and the vertical length for a spherically symmetric atmosphere around the tangent point, where R is the Martian radius. $n(z_0)$ is the density at an arbitary reference altitude z_0.

We assume the absorption cross section is independent on the temperature. The CO_2 cross section at Lyman-alpha for T=195 K and T =295 K can be found in Quémerais et al. 2006 (Fig. 17). At 121.6 nm,the relative difference is small ~ 0.2%, so we could expect a small effect on our results compared to other source of uncertainties.

This relation shows that the expected transmission function can be fitted by a function given by

$$f(z) = \exp\left\{-A\sqrt{H}\exp\left[-\frac{(z-z_0)}{H}\right]\right\} \qquad (4)$$

A and z_0 are not independent, and therefore z_0 can be fixed arbitrarily (here to 110 km) without losing generality. Changing z_0 will provide exactly the same fit, since A would be adjusted to produce the same transmission function.

From A we can derive the CO_2 density at z_0, and from H we can derive the average temperature of the 100 – 160 km layer and above.

We use a Levenberg-Marcquard fit, using the IDL fit package from Markwardt (2009) to derive the best fit of the observed transmission functions for each of the 33 orbits. For each orbit, we perform a Monte Carlo error analysis by adding a random noise to the observed transmission, following a gaussian law $\exp(-\delta T^2/2\sigma^2)$ where σ is the standard deviation on the transmission between 40 – 80 km (~0.05). From 1000 random profiles, we derive the values of the two free parameters with the fit procedure described above. The 1000 best fits of the transmission obtained for orbit 7178 are shown in Fig. 3. From this sample, the median, first and last deciles of the free parameters are considered as the best fit values, and the uncertainties on the parameters. For each orbit, the altitude *z* where $\tau_{CO2} = 1$ (corresponding to a slant CO_2 density of $1.6\text{x}10^{19}$ cm^{-2}) can therefore be calculated.

To estimate the uncertainty associated to the non_isothermal assumption, we have numerically computed the transmission function for non isothermal cases using the temperature profiles from the Mars Climate Database (MCD) or from Groller et al. (2018). We then applied the same retrieval method to the computed transmission function. The uncertainty on the altitude where $\tau = 1$ due to the non-isothermal assumption is estimated to be lower than 2 km.

3) Results

The altitude where CO_2 optical thickness is equal to 1 and the temperature of the absorption layer are displayed in Figure 4. The CO_2 density at 110 km derived from the best fit temperature as well as from an assumed constant temperature of 135 K for all observations are also shown.

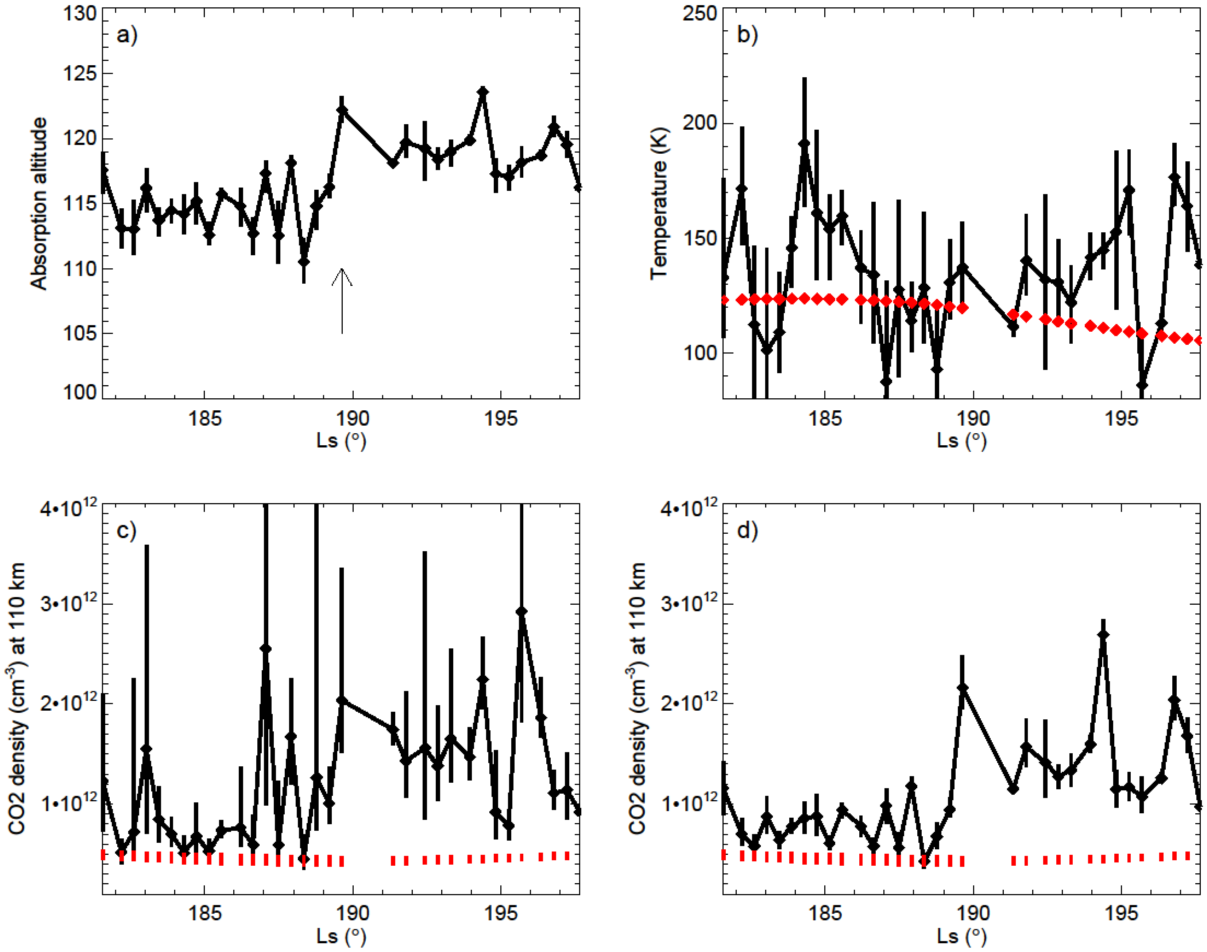

Fig. 4 a) Variations of the CO_2 absorption altitude (km), defined as the altitude where the slant CO_2 absorption optical thickness at Lyman-α is equal to 1 with the solar longitude Ls. b) derived temperature for each orbit from the CO_2 scale height. c) variations of the CO2 density with Ls considering the temperature derived from the fit. d) Same as c) but using a same temperature of 135 K for the full period.The range of temperature and CO_2 density at 110 km extracted from the Mars Climate Database at the same position are shown by red lines for panels 3b, 3c and 3d. The arrow on panel 3a indicate the time of orbit #7182.

The altitude where the CO_2 optical thickness is equal to 1 is almost constant before orbit #7182 (114.5 km with a standard deviation of 2 km) and increases to 119.0 km (standard deviation of 2 km) for the period starting with orbit 7182. The uncertainty on the mean value is 0.5 km for both periods. Orbit 7182 occurred on 8 of June 2018 corresponding to the time where the increase of the dayside CO_2 density at 150 km was observed from the navigation camera (NAVCAM) of

MAVEN (Bougher et al., 2019) and IUVS dayglow emissions (Jain et al., this issue). This increase is associated with the heating of the lower atmosphere by the global dust storm.

The derived temperature is within the range expected for the deep nightside thermosphere (e.g. Forget et al. 2009, Gröller et al. 2018). The derived uncertainties are ~ 30K and are consistent with the range of temperature variations derived from stellar occultations (Forget et al. 2009, Groller et al 2018). The average temperature derived from the full set of observations is 135 K with a standard deviation of 25 K similar to the uncertainty derived from the fits. The average temperature before orbit 7182 is 133K with a standard deviation of 28K and for the period starting with orbit 7182, the average value is 136K with a standard deviation of 23 K. This variation seems different from the temperature decrease predicted by the MCD. Given the large uncertainty on the derived temperature it is not possible to attribute this difference to the global dust storm. It is not possible from our observations to conclude if the orbit to orbit variations of the temperature is real because the temporal variation of the derived temperature is not different from the derived error bar. We also fit the transmission function for each observation using the value of the average temperature to derive the CO_2 density variations at 110 km (Fig. 4d). In this case, the CO_2 density variations show an increase by a factor ~ 1.9±0.2 after orbit #7178. The average density calculated from all orbits before orbit 7182 is 7.8×10^{11} cm^{-3} and the standard deviation is 2.0×10^{11} cm^{-3} ($5.8 \pm 1.5 \times 10^{-8}$kg/m^3, assuming a CO_2 mixing ratio of 0.96). It increases to $14.7 \pm 4.8 \times 10^{11}$ cm^{-3} ($11.2 \pm 3.6 \times 10^{-8}$ kg/m^3) after orbit 7182, as expected from the increase of the CO_2 absorption layer altitude. CO_2 densities derived before and after 8 of June are in the range of the CO_2 density derived by Forget et al. (2009) near Ls = 180°. Using another temperature changes the derived CO_2 density, but the increase factor is only slightly modified. For example, using a temperature of 120 K – close to the derived nightside temperature at 110 km obtained from stellar occultations by SPICAM in 2004, 2005 and 2006 (Forget et al. 2009) – we obtain a CO_2 density increase from $9.0\pm2.4x10^{11}$ cm^{-3} to $18.3\pm6.0x10^{11}$ cm^{-3}.

4) Discussion

A large-scale dust storm was detected in early June by Mars Reconaissance Orbiter (MRO) Mars Color Imager (MARCI) and Mars Climate Sounder (MCS) instruments These instruments associated the dust storm with an increase in lower atmospheric temperature (Zurek et al. 2018, Kass et al. 2018). The first sign of this global dust storm was detected by MAVEN on 8 June (orbit #7184) in the dayside thermosphere. MAVEN accelerometers detected an enhancement in dayside CO_2 density at 150 km by a factor ~ 2 (Zurek et al. 2018) in agreement with the density variations observed by the NAVCAM and NGIMS instruments (Elrod et al. this issue, Bougher et al. 2019). From dayglow observations, IUVS observed an increase in the altitude of peak brightness of 5 to 8 km (Jain et al. this issue). This variability is in agreement with the derived variability measured at the nightside for the observations presented in this study.

The atmospheric mass density measured by the NAVCAM was ~ 0.25-0.3 kg/km^3 at 150 km before the 8 of June and ~0.4-0.55 kg/km^3 after MAVEN orbit 7184 (Bougher et al., 2019). At such altitudes, assuming a CO_2 mass mixing ratio between 0.7 and 0.9, we convert the atmospheric mass density to CO_2 number density between 2.3 - $3.7x10^9$ cm^{-3} and between 3.8 and $6.8x10^9$ cm^{-3} before and during the dust storm, respectively. To compare these values to the derived values in this study requires extrapolating the density derived at 110 km to 150 km. Assuming an isothermal layer between 110 and 150 km and a temperature of 135 K results in a nightside CO_2 density of $3.2x10^9$ cm^{-3} and $6.1x10^9$ cm^{-3} at 150 km, close to the dayside CO_2 density. Considering a temperature of 120 K gives respective CO_2 densities of $2.0x10^9$ cm^{-3} and $4.0x10^9$ cm^{-3}, lower than the dayside derived density. However, NAVCAM shows a decrease of the density at 150 km when MAVEN periapsis is moving from the dayside to the nightside (Bougher et al. 2019), and therefore a temperature of 120 K at the nightside between 110 and 150 km would provide better agreement between the two sets of observations. A possible bias on our retrieved density is the uncertainty in the tangent altitude due to the uncertainty in the real pointing (Chaufray et al. 2011). During the observations presented above, the typical distance between the spacecraft and the tangent point is ~ 5000 km. The IUVS spatial bins (corresponding to a binning of 115 physical pixels along the slit) projection at the tangent point is large ~ 20 km. A systematic change of ±10 km on the altitude of the tangent point would increase/decrease all the derived CO_2 densities at 110 km by a factor ~4. But in both cases, the ratio of the density during and before the dust storm would not be modified if these effects are systematic.

5) Summary and conclusion

IUVS observations of the Lyman-α hydrogen line in the Martian lower thermosphere show an increase in the altitude of absorption layer of the Lyman-α emission by CO_2 on 8 June 2018, coincident with the expansion of the dayside thermosphere observed by several MAVEN instruments. This increase is most likely associated with the large-scale dust storm observed by MRO few days before that heated the lower atmosphere. This altitude variation is attributed to an increase of the CO_2 density by a factor ~ 1.9±0.2 assuming an isothermal atmosphere between 100 and 160 km. While the absolute derived density is sensitive to the accuracy of the pointing and the assumed temperature, the relative variation in density is not. We can estimate the global heating of the lower atmosphere needed to produce such an increase of the density. Assuming a moderately deep region (ΔZ = 50 km) of uniform heating and a constant surface pressure. The increase of the CO_2 density at 110 km is related to the increase of the vertically average scale height $\langle H \rangle$ by

$$\beta = \frac{<H>_2}{<H>_1} = \frac{1}{1 - \frac{<H>_1}{\Delta Z} \ln\left(\frac{n_2}{n_1}\right)} \tag{5}$$

$$\frac{1}{<H>_i} = \frac{1}{\Delta Z} \int_0^{\Delta Z} \frac{dz}{H_i(z)}, \tag{6}$$

where, $H_1(z)$ is the atmospheric scale height at z < 50 km before 8 June 2018, $H_2(z)$ the scale height at z < 50 km after 8 june 2018 and n_2/n_1 the observed CO_2 density increase at 110 km, Assuming $<H>_1$ between 8 - 12 km, it leads to an average increase of the temperature between ~10 - 20% (~25 – 50 K) in the lower atmosphere of Mars. This is just an estimate of the heating. Simulations from Global Circulation Models, including the dynamics of the atmosphere are needed to capture the links between the lower atmosphere and the upper atmosphere more accurately. This analysis confirms the global effect of the GDS on the nightside thermosphere of Mars at altitudes not sampled by other instruments and will provide additional constraints to better understand the dynamics and heating distribution associated with such events.

Acknowledgments

This work and the MAVEN project are supported by NASA through the Mars Exploration Program. All IUVS inbound limb (“inlimb”) data used in this paper with revision/version tag v13_r01 are archived in NASA’s Planetary Data System :

http://atmos.nmsu.edu/data_and_services/atmospheres_data/MAVEN/maven_iuvs.html. The parameters extracted from the MCD v5.3 can be found at http://www-mars.lmd.jussieu.fr/mcd_python/index5.html.

J-Y. Chaufray is supported by the Centre National d'Etudes Spatiales. We thanks two anonymous referees for their constructive comments.

References

Bertaux, J-L., F. Leblanc, S. Perrier, E. Quémerais, O. Korablev, E. Dimarellis, A. Réberac, F. Forget, P.C. Simon, S.A. Stern, B. Sandel, and SPICAM team, Nightglow in the upper atmosphere of Mars and implications for atmospheric transport, Science, 307, 566-569, (2005)

Bougher S.W., R.H. Tolson, R.W. Zurek, D.T. Bairn, R. Lugo, and G. Jenkins, MAVEN Aerobraking campaign of 2019 and the resulting accelerometer measurements : wave features in the Martian thermosphere, DPS-EPSC, 2019

Chaufray, J-Y., K.D. Retherford, D.G. Horvath, J-L. Bertaux, F. Forget, and F. Leblanc, The density of the upper martian atmosphere measured by Lyman-α absorption with Mars Express SPICAM, Icarus, 215, 522-525, 2011

Elrod M. et al., this issue

Forget, F., F. Montmessin, J-L. Bertaux, F. Gonzalez-Galindo, S. Lebonnois, E. Quémerais, A. Réberac, E. Dimarellis, and M.A. Lopez-Valverde, Density and temperatures of the upper Martian atmosphere measured by stellar occultations with Mars Express SPICAM.

Fox, J., M.I. Galand, and R.E. Johnson, Energy deposition in planetary atmospheres by charged particles and solar photons., Space Sci. Rev., 139, 3-62, (2008)

Gröller, H.F., R.V. Yelle, T.T. Koskinen, F. Montmessin, G. Lacombe, N.M. Schneider, J. Deighan, A.I.F Stewart, S.K. Jain, M.S. Chaffin and 9 co-authors, Probing the Martian upper atmosphere with MAVEN/IUVS stellar occultations, Geophys. Res. Lett, 42, 9064, (2015)

Gröller, H., F. Montmessin, R.V. Yelle, F. Lefèvre, F. Forget, N.M. .Schneider, T.T. Koskinen, J. Deighan, and S.K. Jain, MAVEN/IUVS stellar occultation measurements of Mars atmospheric structure and composition, J. Geophys. Res., 123, 1449-1483, (2018)

Jain, S. et al., this issue

Kass D.M., A. Kleinboehl, J.H. Shirley, J.T. Schofield, D. McCleese, N.G. Heavens, Overview of the 2018a Global dust event from Mars Climate Sounder Observations, AGU, Fall Meeting 2018, abstract #P34A-02.

Markwardt, C. B. 2009, "Non-Linear Least Squares Fitting in IDL with MPFIT," in proc. *Astronomical Data Analysis Software and Systems XVIII*, Quebec, Canada, ASP Conference Series, Vol. 411, eds. D. Bohlender, P. Dowler & D. Durand (Astronomical Society of the Pacific: San Francisco), p. 251-254 (ISBN: 978-1-58381-702-5; Link to ASP title listing)

McClintock, W.E., N.M. Schneider, G.M. Holsclaw, J.T. Clarke, A.C. Hoskins, F. Montmessin, R.V. Yelle, and J. Deighan, The Imaging Ultraviolet Spectrograph (IUVS) for the MAVEN mission, Space Sci. Rev., DOI 10.1007/s11214-014-0098-7, 2015

Quémerais, E., J-L. Bertaux, O. Korablev, E. Dimarellis, C. Cot, B. Sandel, and D. Fussen, Stellar occultations observed by SPICAM on Mars Express, J. Geophys. Res., 111, E09S04, doi: 10.1029/2005JE002604, 2006

Zurek, R.W., S.W. Bougher, R. Tolson, D. Baird, S. Demcak, D.M. Kass, R. Lugo, and B.M. Jakosky, The Planet-Encircling Dust Storm: Effects on the Mars Upper Atmosphere as seen in MAVEN Accelerometer Data, AGU, Fall Meeting 2018, abstract #P43J-3864

Figure 1.

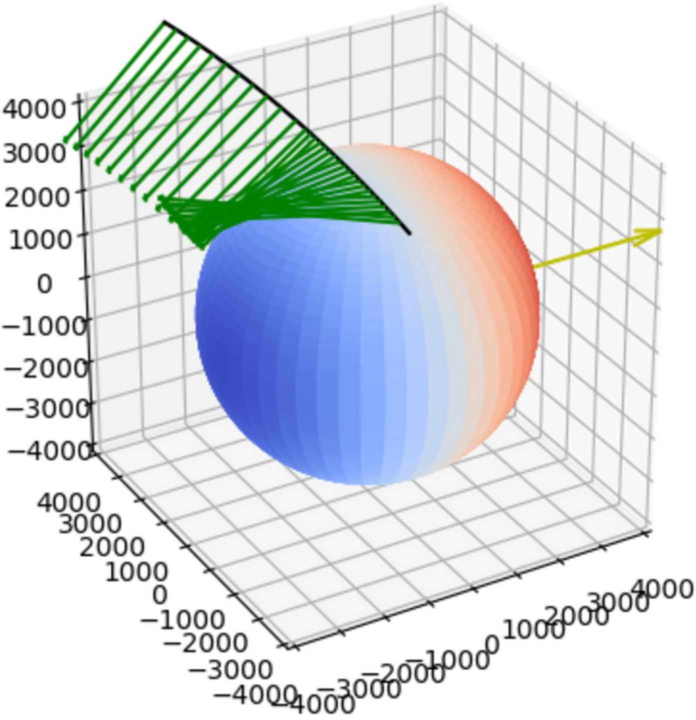

4000
3000
2000
1000
0
−1000
−2000
−3000
−4000
4000
3000
2000
1000
0
−1000
−2000
−3000
−4000
−4000
−3000
−2000
−1000
0
1000
2000
3000
4000

Figure 2.

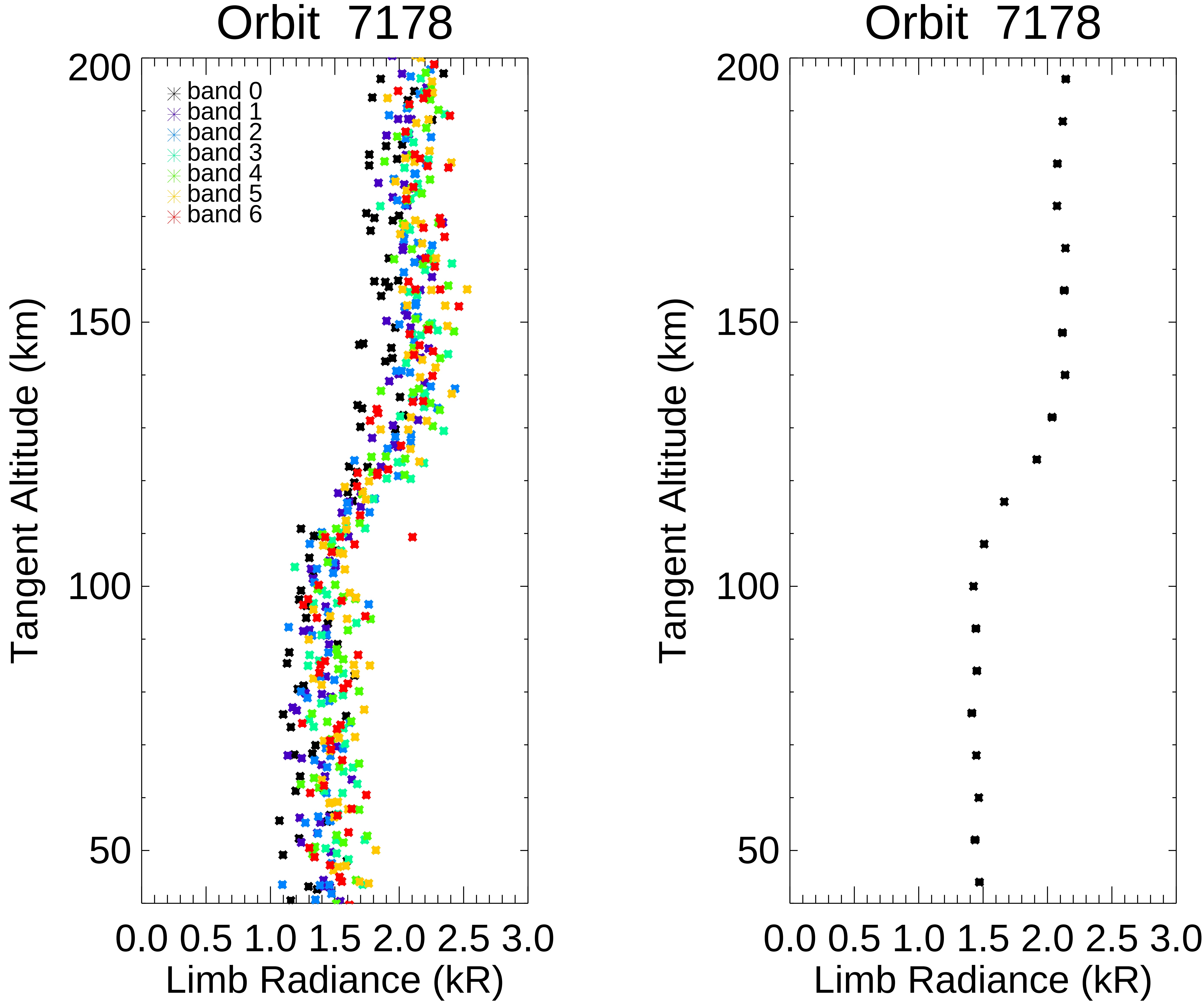
Orbit 7178
200
150
100
50
Tangent Altitude (km)
band 0
band 1
band 2
band 3
band 4
band 5
band 6
0.0 0.5 1.0 1.5 2.0 2.5 3.0
Limb Radiance (kR)
Orbit 7178
200
150
100
50
Tangent Altitude (km)
0.0 0.5 1.0 1.5 2.0 2.5 3.0
Limb Radiance (kR)

Figure 3.

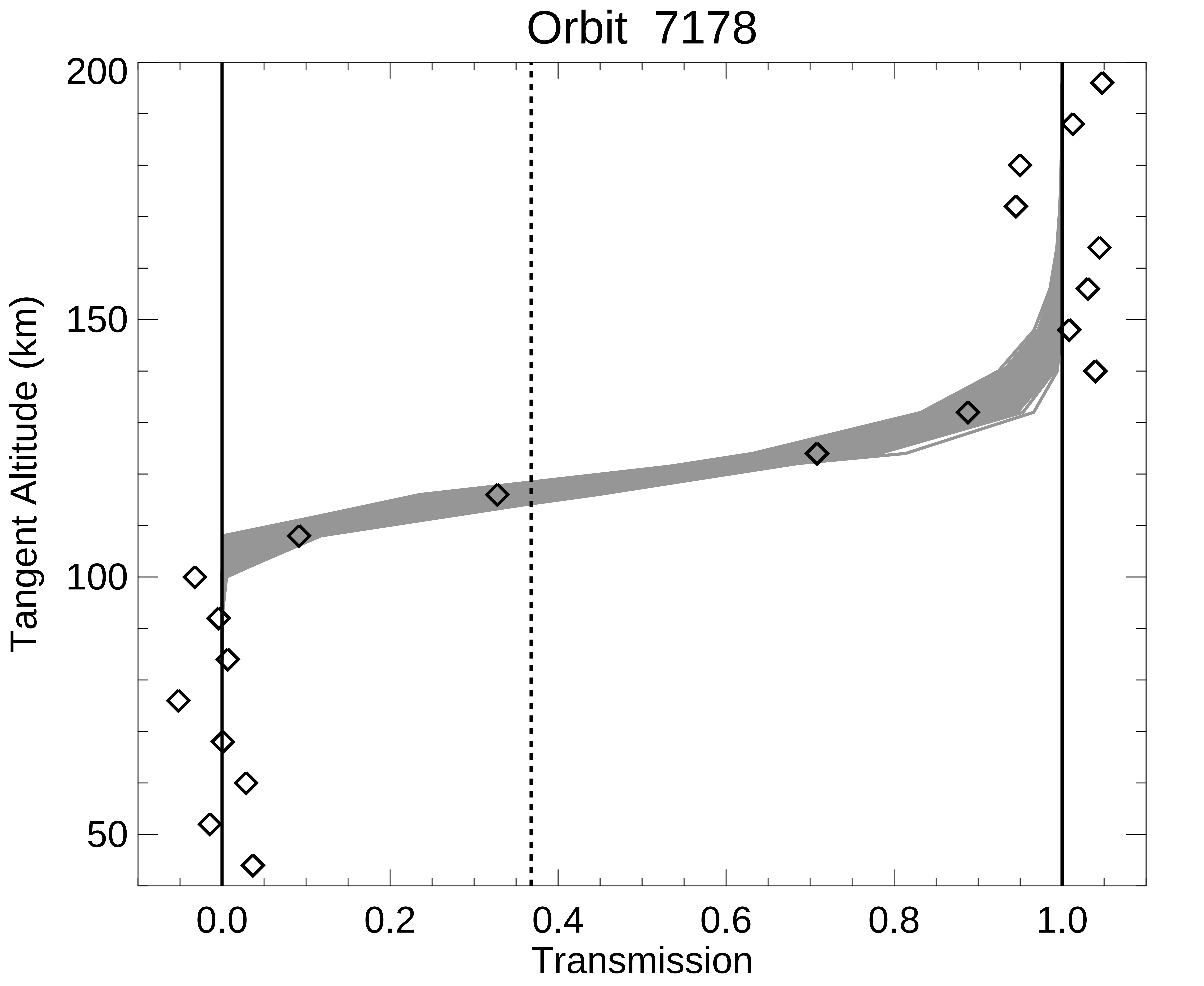
Orbit 7178
Tangent Altitude (km)
200
150
100
50
0.0
0.2
0.4
0.6
0.8
1.0
Transmission

Figure 4.

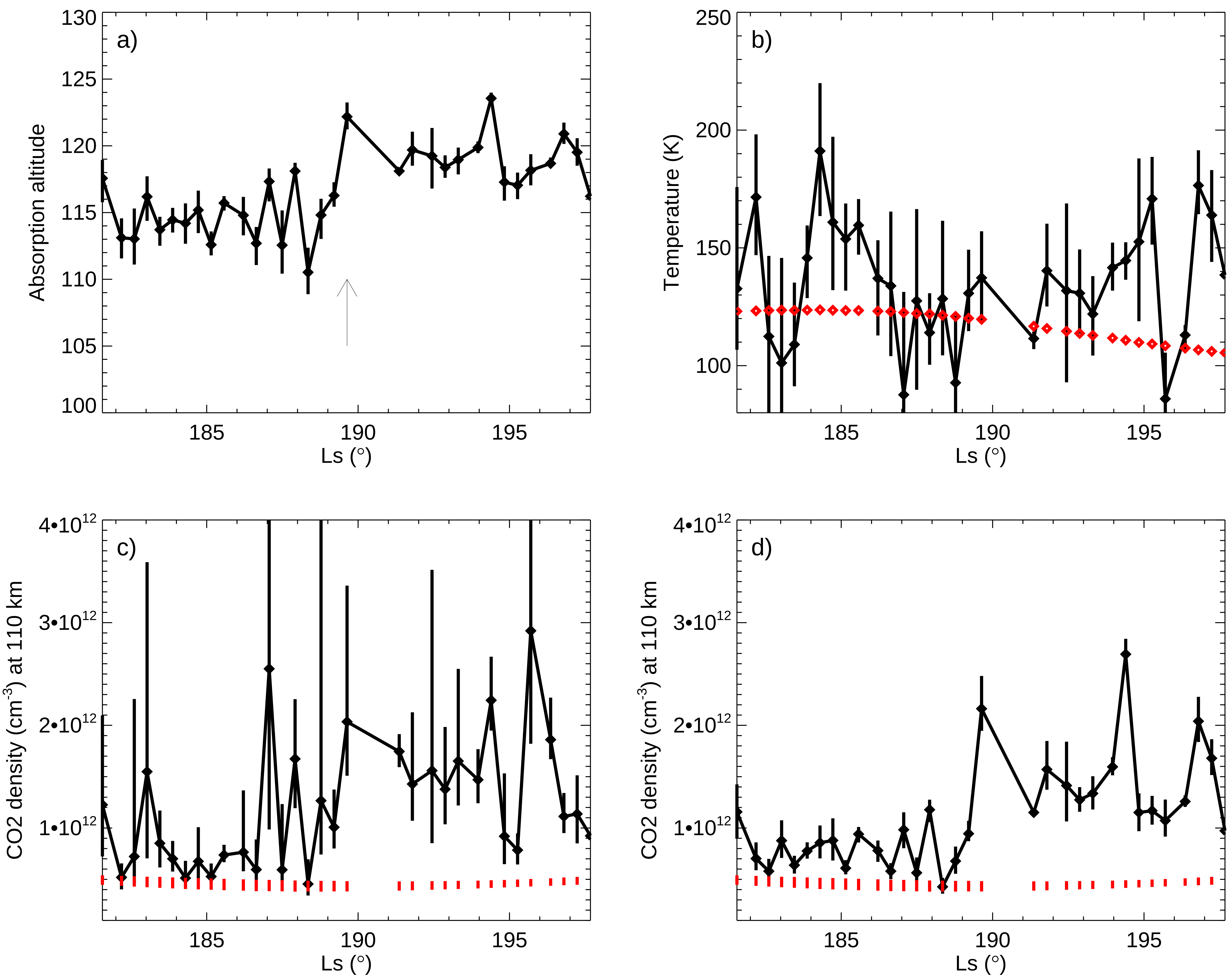

a)
Absorption altitude
130
125
120
115
110
105
100
185
190
195
Ls (°)
b)
Temperature (K)
250
200
150
100
c)
CO2 density (cm^{-3}) at 110 km
4•10^{12}
3•10^{12}
2•10^{12}
1•10^{12}
d)